Electronic Supplementary Material (ESI) for Physical Chemistry Chemical Physics.

Electronic Supplementary Information

Elucidating Low-Frequency Vibrational Dynamics in Calcite and Water with Time-Resolved Third-Harmonic Generation Spectroscopy

Liang Wang,[1,†] *Weimin Liu,*[1,†] *and Chong Fang*[1,2,*]

[1] Department of Chemistry, Oregon State University, Corvallis, Oregon 97331, USA

[2] Center for Sustainable Materials Chemistry, Oregon State University, Corvallis, Oregon 97331, USA

[†] These authors contribute equally to this work.

Corresponding Author

* To whom correspondence should be addressed: Chong.Fang@oregonstate.edu

TOC Page number

SI Text

SI Figures

Additional **discussions** follow each Figure caption

SI Text

Additional discussion on the lower-frequency phonons in calcite. In principle, an optical phonon can split into two phonons (three-phonon process) or three phonons (four-phonon process) with lower frequencies (down-conversion). It is also possible that a phonon turns into a higher-frequency phonon when scattered by a thermal phonon (up-conversion).[1] There are many channels for a phonon to decay in condensed phase, but the probability of high-order process (more than three-phonon process) and up-conversion is negligible compared to three-phonon, down-conversion process.[2] Therefore, more probable decay channels could explain the ~250 fs lifetime of the observed 703 cm^{-1} mode in crystalline calcite. The shoulder peak at ~125 cm^{-1} (near the 155 cm^{-1} mode) in the FFT spectrum of TRTHG intensity quantum beats within 4 ps (Fig. 2c) corresponds to an IR-active mode[3] in calcite and may not be directly excited by FP1 (the incident fs pump pulse, Scheme 1) via a Raman process. We conjecture that it originates from anharmonic decay of higher-frequency phonons. Two possible pathways are listed below,

$282\ cm^{-1} \rightarrow 155\ cm^{-1} + 127\ cm^{-1}$

$155\ cm^{-1} \rightarrow 127\ cm^{-1}$ + acoustic or thermal phonon(s)

These energy relaxation processes may also contribute to the small interference effect observed in the time-resolved intensity decay profiles of the 155 and 282 cm^{-1} modes (Fig. 2d), where a relatively lower (higher) frequency optical phonon mode is anharmonically coupled to the former (latter) mode, respectively. These spectral intensity modulations on the fs to ps timescale due to anharmonic coupling have been observed in photoacids and fluorescent proteins in solution.[4-6]

Additional discussion on the vibrational quantum beats in TRTHG. Double-sided Feynman diagrams of the involving nonlinear processes in impulsive stimulated Raman scattering (ISRS)

upon interaction with FP1 are shown in Scheme 2. The third-order THG signal is emitted in the $\bar{k}_1 + 2\bar{k}_2$ phase-matching direction, while FP1 also generates an electronic coherence in the condensed medium that is represented by $|e\rangle$ from the electronic ground state $|g\rangle$. It is notable that our spectral data analysis (see Fig. 2 for example) effectively separates the coherent *vibrational* quantum beats from the free induction decay (FID) of the *electronic* resonance-based time-delayed THG signal, which are confirmed by the third-order nature of the THG signal "carrier" wave (power dependence on incident pulse energies shown in Fig. 1) and the power dependence of the $\chi^{(3)}$-induced oscillation amplitude on the first incident pump pulse energy (see Fig. S3 below). The impulsively generated electronic and phonon states may be delocalized in the sample medium following photoexcitation so the nonlinear processes do not necessarily concentrate on one molecule *per se*, making it possible to observe the modulation of the time-resolved third-order THG signal strength by the low-frequency vibrational motions generated in the medium via the ISRS process. This modulation mechanism is mainly based on the time-dependent cubic nonlinear polarizability $\chi^{(3)}(t)$ (see eqn (1) in the main text) and the resultant THG signal power expression: $I_{THG} \propto (\chi^{(3)} E_1 E_2^{\,2})^2 = [\chi^{(3)}]^2 \cdot I_1 I_2^{\,2}$.

In other words, the impulsively excited coherent phonon modes evolve on the electronic ground state S_0, which modulates the time-resolved THG signal via the cubic electric susceptibility $\chi^{(3)}$ consisting of the Raman polarizability tensor. This type of transient nonlinear light-matter interaction mechanism is similar to the vibrational quantum beats that we discovered using femtosecond stimulated Raman spectroscopy (FSRS) in solvated photoacids,[5,7,8] fluorescent proteins,[4] and fluorescent protein biosensors.[6,9,10] No higher-order signal power dependence was observed in those experiments either because the actinic photoexcitation pulse is femtosecond in time duration and generates the low-frequency vibrational coherences, which

evolve in the electronically excited potential energy surface to be subsequently probed by the stimulated Raman pump-probe pair.[4,6,11,12] In this work, the measured THG signal and quantum beating amplitude show different dependence on the power of two incident pulses and the first incident pulse, respectively, confirming that the interplay between a *separate* ISRS process and the time-resolved THG signal generation is responsible for the observed vibrational quantum beats that persist on the fs to ps timescale. Notably, this phenomenon depends on the local microenvironment that affects the coherence damping rate of the anharmonic oscillators in the condensed medium, while the electronic coherence and vibrational coherence do not need to concentrate on a single molecule at the exact same time.

Additional discussion on the resolving power of TRTHG spectroscopy. In general, coherent phonon spectroscopy is highly sensitive to microstructures.[13-15] The observed difference in low-frequency vibrational mode position and lifetime between pure water and water with 4 M $ZnCl_2$ solute (see main text) demonstrates the high sensitivity of our TRTHG technique to distinguish local molecular environment (e.g., H-bonding configuration within the first solvation shell of the spectral probe)[16-18] on the femtosecond timescale that starts to relax toward thermal equilibrium.[7] Notably, the THG signal is time-resolved so at later time delay, e.g., on the ps timescale, the first pump pulse k_1 is gone but we still observe the THG signal due to transient macroscopic polarization mainly from electronic resonance near the fundamental of the 800 nm pulse (i.e., electric oscillating dipoles from the sample medium transient response, and potentially some polariton contribution).[19,20] The third-order THG signal is also dependent on the nonlinear optical susceptibility and polarizability $\chi^{(3)}$ of the medium that is temporally modulated by the damped coherent phonon modes, which are generated by the pump pulse k_1 via ISRS process.[11,21,22]

At the core of this significant advance is the interplay between light and the electronic and vibrational forces in condensed matter, from solid, liquid, to salt solution, and the pronounced coherent quantum beats readily observed in the background-free, non-invasive, ubiquitous, and high sensitivity THG signal. Our versatile setup differs significantly from existing nonlinear methods such as surface second-harmonic generation, or time-resolved pump-probe wherein the reflectivity or transmission changes of the probe pulse is measured.[23-25] The conformational dynamics snapshot pertaining to impulsively excited coherent phonon modes provides deep insight into the fundamental mechanism of heat and electron transport in functional materials.[26-28] The simplicity and robustness of THG signal generation and subsequent data analysis, together with surface specificity to be highly sensitive to interfacial boundaries,[29-31] make TRTHG an alternative powerful spectroscopic methodology that a broad community can implement to unravel low-frequency molecular structural dynamics in condensed phase and in real time.

SI Figures

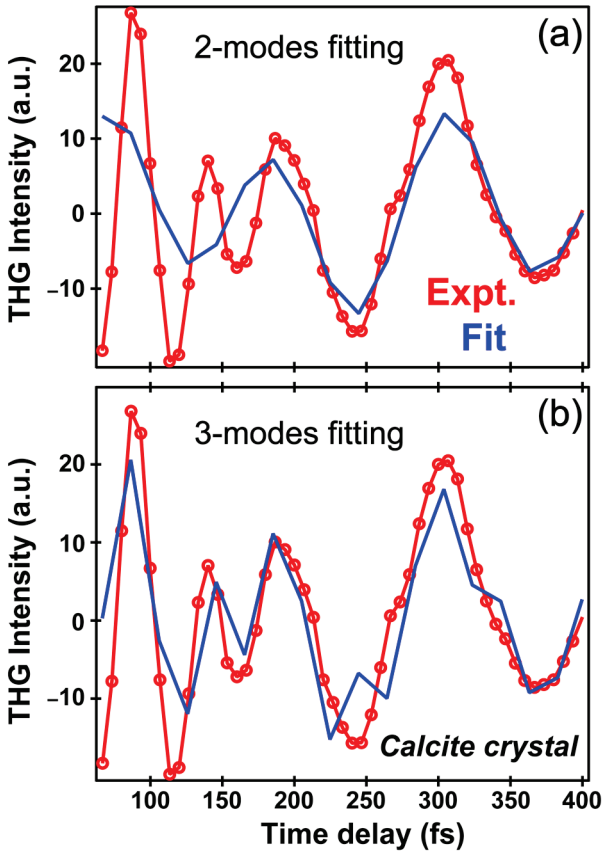

Fig. S1 Comparison between the (a) 2-modes and (b) 3-modes decaying sine wave fitting of the intensity quantum beats in the TRTHG data of crystalline calcite within 400 fs after FP1 excitation. The experimental THG intensity data (red circle line) is overlaid with the least-squares-fitting results (blue solid curve) in each case based on eqn (2) (see main text). It is apparent that the 3-modes fitting significantly improves the match between measured and fitted curves particularly on the early timescale (i.e., within 400 fs), corroborating the validity of this mathematical approach to retrieve a minimal set of underlying low-frequency (optical) phonon modes that modulate the observed background-free THG signal on the ultrafast timescale.

In (a), the fitting result yields two phonons at ~156 and 283 cm^{-1} with the lifetime of ~1.7 and 1.3 ps, respectively. The relative amplitude weight of the two modes is ~31% and 69%. In

(b), the fitting result yields three phonons at ~155, 282, and 692 cm^{-1} with the lifetime of ~1.6 ps, 1.3 ps, and 250 fs, respectively. To find the physically meaningful lifetime for the least determined and weakest ~692 cm^{-1} mode, the observed peak width (i.e., 25 cm^{-1}) in Fig. 2c is used as a constraint during the least squares numerical fitting of the convoluted quantum beats (see Fig. 2b). Since the 692 cm^{-1} mode in this data set (the main text reports the average value of 703 cm^{-1} from fitting multiple data sets collected on different days) only affects the early time coherent oscillations, the relative amplitude weight of the two modes (i.e., 155 and 282 cm^{-1}) with ps decay time constants is calculated at ~30% and 70%, almost unchanged from the 2-modes fitting case. This indicates that the two robustly determined lower-frequency modes (i.e., < 300 cm^{-1}) are largely responsible for the overall THG quantum beating on the sub-ps to ps timescale (Fig. 2a, b) because their associated lattice atomic motions as discussed in the main text significantly modulate the third-order electric nonlinear susceptibility $\chi^{(3)}$ of the medium.[32,33] Their longer lifetime in S_0 on the ps timescale ensures that their modulation of the THG electric carrier wave is detected with high sensitivity and a larger time window than the associated free induction decay (FID) of electronic resonance (e.g., as shown by the double-exponential fit of the THG signal intensity temporal profile in Fig. 2a), so the determination of their vibrational dynamics is more accurate than that of the ephemeral 692 cm^{-1} mode. The larger amplitude weight of the 282 cm^{-1} mode is also consistent with its higher Raman intensity (see Fig. 2c).[34]

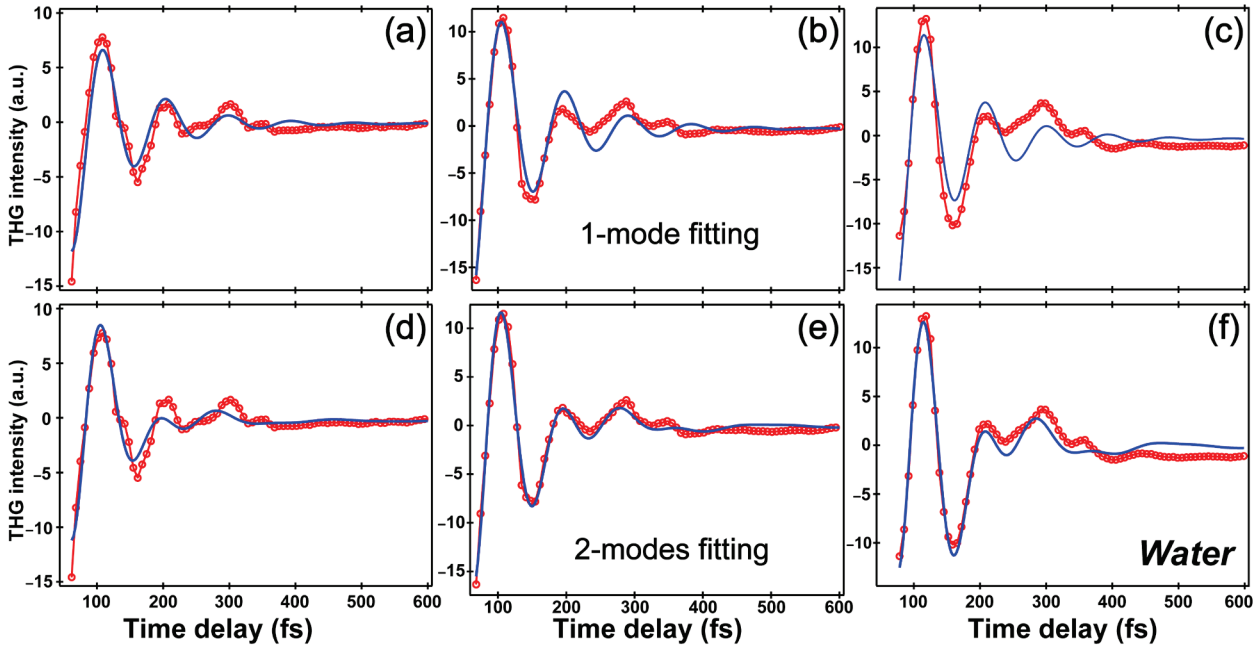

Fig. S2 Comparison between the 1-mode and 2-modes decaying sine wave fitting (blue solid curve) of the TRTHG intensity quantum beats (red circle line) of pure water. In the upper panels to demonstrate experimental reproducibility, (a), (b), and (c) show the THG intensity quantum beats collected on three different days, overlaid with the single-mode sine wave fitting reporting 352 cm^{-1} (87 fs lifetime), 360 cm^{-1} (88 fs lifetime), and 360 cm^{-1} (89 fs lifetime), respectively. In the lower panels, (d), (e), and (f) show the vertically corresponding experimental data overlaid with double-modes sine wave fitting results. It is apparent that the 2-modes fitting improves the accuracy to simulate the observed temporal oscillations of the THG signal intensity, particularly within the 200—600 fs time window (i.e., coherent modulation by a lower-frequency mode).[5]

In (d), the fitted mode parameters are 180 cm^{-1} (115 fs lifetime, 16% amplitude relative weight) and 380 cm^{-1} (60 fs lifetime, 84% amplitude relative weight). In (e), the fitted mode parameters are 148 cm^{-1} (142 fs lifetime, 12% amplitude relative weight) and 384 cm^{-1} (68 fs lifetime, 88% amplitude relative weight). In (f), the fitted mode parameters are 154 cm^{-1} (125 fs

lifetime, 22% amplitude relative weight) and 391 cm^{-1} (70 fs lifetime, 78% amplitude relative weight). On average, the two low-frequency modes retrieved from this 2-mode least squares fitting analysis, ca. 160 and 385 cm^{-1}, match well with our ground-state FSRS data showing two broad peaks at ca. 180 and 390 cm^{-1} for pure water (see Fig. 4a). The observed lower-frequency mode is commonly attributed to the intermolecular O–H···O hydrogen bond (H-bond) stretching motion (translational),[35] while the 390 cm^{-1} mode corresponds to a librational motion (hindered rotation).[16,17,35] The fitted lifetime of ~130 fs of the H-bond stretching mode[18] is longer than the ~70 fs lifetime of the 385 cm^{-1} librational mode, which is consistent with the mode composition that the latter (hindered rotation) is more susceptible to local fluctuations with more spatial degrees of freedom in an extended H-bonding network in pure water hence coherence damping due to phase-randomizing collisions.[36] This mechanistic interpretation is corroborated by the observation that the vibrational mode at ca. 390 cm^{-1} is broader than the 180 cm^{-1} mode in water (Fig. 4a).

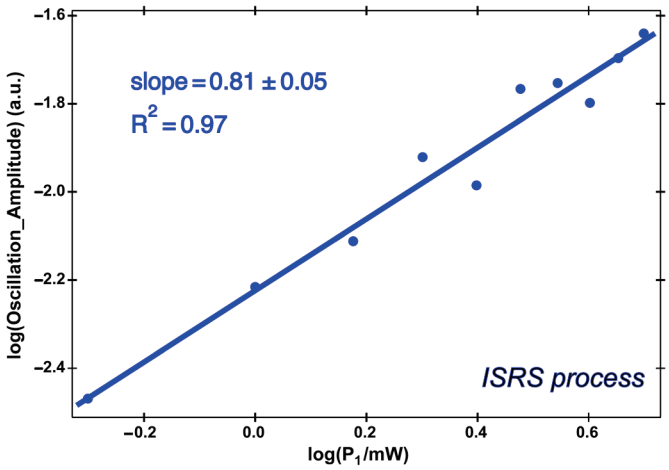

Fig. S3 Power dependence of the observed quantum beats as seen in Fig. 2b for 1-mm-thick polycrystalline calcite. The dynamic THG signal emitted in the $\vec{k}_1 + 2\vec{k}_2$ direction is measured using a Si photodiode and lock-in amplifier at different time delay between the two incoming pulses (details in Experimental Section). The incident FP1 power (P_1) is increased from 0.5 to 5 mW with 0.5 mW increments. The other incident FP2 power is maintained at 1 mW. After double-exponential fitting the decaying THG intensity traces, the time-resolved oscillatory component is extracted as the residual (e.g., see Fig. 2b). Half of the observed intensity difference between the first (also the largest) oscillatory peak and dip is taken as the initial quantum beating amplitude. This amplitude scales linearly ($0.81 \approx 1$) with the FP1 power.

Given that the FID of the electronic resonance leads to small THG signal magnitude in this regime (i.e., signal beyond ~60 fs) sitting on top of a constant background (e.g., Fig. 2a), the retrieved vibrational quantum beating amplitude after subtracting the THG signal decay profile is found to be roughly linear to the incident FP1 power. Scheme 1 shows that FP1 is the pulse being chopped in the noncollinear pump-probe geometry. This experimental result bolsters our understanding of the observed phonon motions originating from the ISRS process (see main text

and Scheme 2) by two field interactions with the first incident pump pulse (FP1). There is extensive literature on underlying mechanisms for coherent optical phonon mode generation using femtosecond laser pulses[11,21,22] with the consensus that the impulsive Raman contribution is proportional to the number density of oscillators (i.e., effective concentration of impulsively excited low-frequency vibrational modes) and the vibrational amplitude, which can be approximated as the following expression, $P_{Raman} = N\left(\partial\alpha/\partial Q\right)\cdot QE$, where N represents the effective concentration of vibrational oscillators, the differential polarizability tensor $\left(\partial\alpha/\partial Q\right)$ stands for the molecular linear polarizability change with respect to the vibrational coordinate Q, and E is the incident electric field (i.e., FP1 in our experiment).[21,22,36] Assuming that the femtosecond FP1 is not depleted by stimulated scattering and the incident pulse duration is small compared to vibrational period, the vibrational oscillator is driven by the force quadratic in the field of E, which exerts a spatially uniform, temporally impulsive driving force on Raman-active vibrational modes (e.g., those solid-state optical phonon modes in Fig. 2 and low-frequency vibrational modes in solution as shown in Fig. 3). As a result, the retrieved vibrational quantum beating amplitude goes approximately as the first power of FP1 intensity,[19] which confirms the impulsive nature of these observed optical phonon modes that depend on the initial FP1 excitation but not the time-delayed, unchopped FP2 (see Scheme 1).

SI References:

1. S. Yang, S. Adhikari, M. Dobbala and F. Ganikhanov, *Appl. Phys. Lett.*, 2011, **99**, 221903.

2. S. K. Estreicher, T. M. Gibbons, B. Kang and M. B. Bebek, *J. Appl. Phys.*, 2014, **115**, 012012.

3. M. Prencipe, F. Pascale, C. M. Zicovich-Wilson, V. R. Saunders, R. Orlando and R. Dovesi, *Phys. Chem. Minerals*, 2004, **31**, 559-564.

4. C. Fang, R. R. Frontiera, R. Tran and R. A. Mathies, *Nature*, 2009, **462**, 200-204.

5. W. Liu, F. Han, C. Smith and C. Fang, *J. Phys. Chem. B*, 2012, **116**, 10535-10550.

6. B. G. Oscar, W. Liu, Y. Zhao, L. Tang, Y. Wang, R. E. Campbell and C. Fang, *Proc. Natl. Acad. Sci. U.S.A.*, 2014, **111**, 10191-10196.

7. F. Han, W. Liu and C. Fang, *Chem. Phys.*, 2013, **422**, 204-219.

8. Y. Wang, W. Liu, L. Tang, B. G. Oscar, F. Han and C. Fang, *J. Phys. Chem. A*, 2013, **117**, 6024-6042.

9. L. Tang, W. Liu, Y. Wang, Y. Zhao, B. G. Oscar, R. E. Campbell and C. Fang, *Chem. Eur. J.*, 2015, **21**, 6481-6490.

10. Y. Wang, L. Tang, W. Liu, Y. Zhao, B. G. Oscar, R. E. Campbell and C. Fang, *J. Phys. Chem. B*, 2015, **119**, 2204-2218.

11. P. Kukura, D. W. McCamant and R. A. Mathies, *Annu. Rev. Phys. Chem.*, 2007, **58**, 461-488.

12. R. R. Frontiera, C. Fang, J. Dasgupta and R. A. Mathies, *Phys. Chem. Chem. Phys.*, 2012, **14**, 405-414.

13. W. A. Kutt, W. Albrecht and H. Kurz, *IEEE J. Quantum Electron.*, 1992, **28**, 2434-2444.

14. J. Qi, X. Chen, W. Yu, P. Cadden-Zimansky, D. Smirnov, N. H. Tolk, I. Miotkowski, H. Cao, Y. P. Chen, Y. Wu, S. Qiao and Z. Jiang, *Appl. Phys. Lett.*, 2010, **97**, 182102.

15. W. Liu, L. Wang, F. Han and C. Fang, *Appl. Phys. Lett.*, 2013, **103**, 201116.

16. C. J. Fecko, J. D. Eaves, J. J. Loparo, A. Tokmakoff and P. L. Geissler, *Science*, 2003, **301**, 1698-1702.

17. J. Petersen, K. B. Møller, R. Rey and J. T. Hynes, *J. Phys. Chem. B*, 2013, **117**, 4541-4552.

18. J. Savolainen, S. Ahmed and P. Hamm, *Proc. Nat. Acad. Sci. U.S.A.*, 2013, **110**, 20402-20407.

19. T. F. Crimmins, N. S. Stoyanov and K. A. Nelson, *J. Chem. Phys.*, 2002, **117**, 2882-2896.

20. A. D. Jameson, J. L. Tomaino, Y.-S. Lee, G. Khitrova, H. M. Gibbs, C. N. Böttge, A. C. Klettke, M. Kira and S. W. Koch, *Optica*, 2014, **1**, 276-280.

21. Y.-X. Yan, E. B. Gamble and K. A. Nelson, *J. Chem. Phys.*, 1985, **83**, 5391-5399.

22. A. Nazarkin and G. Korn, *Phys. Rev. A*, 1998, **58**, R61-R64.

23. G. C. Cho, W. Kutt and H. Kurz, *Phys. Rev. Lett.*, 1990, **65**, 764-766.

24. Y. M. Chang, L. Xu and H. W. K. Tom, *Phys. Rev. Lett.*, 1997, **78**, 4649-4652.

25. Y. R. Shen, *J. Opt. Soc. Am. B*, 2011, **28**, A56-A66.

26. O. Delaire, J. Ma, K. Marty, A. F. May, M. A. McGuire, M. H. Du, D. J. Singh, A. Podlesnyak, G. Ehlers, M. D. Lumsden and B. C. Sales, *Nat. Mater.*, 2011, **10**, 614-619.

27. A. J. Minnich, J. A. Johnson, A. J. Schmidt, K. Esfarjani, M. S. Dresselhaus, K. A. Nelson and G. Chen, *Phys. Rev. Lett.*, 2011, **107**, 095901.

28. D. G. Cahill, P. V. Braun, G. Chen, D. R. Clarke, S. Fan, K. E. Goodson, P. Keblinski, W. P. King, G. D. Mahan, A. Majumdar, H. J. Maris, S. R. Phillpot, E. Pop and L. Shi, *Appl. Phys. Rev.*, 2014, **1**, 011305.

29. D. Kupka, J. W. Wilson, O. Masihzadeh and R. A. Bartels, *Chem. Phys. Lett.*, 2010, **490**, 97-101.

30. W. Liu, L. Wang, F. Han and C. Fang, *Opt. Lett.*, 2013, **38**, 3304-3307.

31. L. Zhu, W. Liu and C. Fang, *Appl. Phys. Lett.*, 2013, **103**, 061110.

32. R. Merlin, *Solid State Commun.*, 1997, **102**, 207-220.

33. M. Born and K. Huang, *Dynamical Theory of Crystal Lattices*, Oxford University Press, USA, New York, NY, 1998.

34. S. Gunasekaran, G. Anbalagan and S. Pandi, *J. Raman Spectrosc.*, 2006, **37**, 892-899.

35. D. M. Carey and G. M. Korenowski, *J. Chem. Phys.*, 1998, **108**, 2669-2675.

36. J. L. McHale, *Molecular Spectroscopy*, Prentice-Hall, Upper Saddle River, NJ, 1999.